ChemistrySelect

Research Article
doi.org/10.1002/slct.202300274

Chemistry Europe
European Chemical Societies Publishing

www.chemistryselect.org

Donor Influence on the Optoelectronic Properties of N-Substituted Tetraphenylimidazole Derivatives

Tomas Matulaitis,[a] Paloma L. dos Santos,[b, c] Youichi Tsuchiya,[d] David B. Cordes,[a] Alexandra M. Z. Slawin,[a] Chihaya Adachi,[d] Ifor D. W. Samuel,*[b] and Eli Zysman-Colman*[a]

Three new 1,2,4,5-tetraphenylimidazole derivatives, 9,9-dimethyl-10-(4-(2,4,5-triphenyl-1H-imidazol-1-yl)phenyl)-9,10-dihydroacridine (**DMAC-TPI**), 10-(4-(2,4,5-triphenyl-1H-imidazol-1-yl)phenyl)-10H-phenoxazine (**PXZ-TPI**), and 10-(4-(2,4,5-triphenyl-1H-imidazol-1-yl)phenyl)-10H-phenothiazine (**PTZ-TPI**), bearing different electron donors at the N1 position of the imidazole were synthesised and characterised. **DMAC-TPI** and **PXZ-TPI** showed narrow emission at λ_{PL} of 388 and 418 nm in toluene, and in doped films in Zeonex polymer (1 wt.%) at λ_{PL} 381 and 407 nm, respectively, with a full width at half maximum (FWHM) ranging 0.42-0.44 eV. **DMAC-TPI** and **PXZ-TPI** are predicted to show very low oscillator strength for the low-energy transitions, which aligns to the observed low photoluminescence quantum yields. Both molecules showed a singlet-triplet energy gap (ΔE_{ST} of around 1.2 eV) that is much too large to enable reverse intersystem crossing and thermally activated delayed fluorescence. Connecting a donor group to **TPI** at the N1 position can lead to room temperature phosphorescence (RTP), as the example of **PTZ-TPI** showed.

Introduction

Organic light-emitting diodes (OLEDs) as a display technology can now be found in many different sized consumer electronics from smartwatches to mobile phones to tablet and laptop displays, and large-area televisions.[1] OLEDs offer several advantages compared to inorganic light-emitting diodes (LEDs), such as the ability to be fabricated on flexible substrates, their low operational voltage, high contrast ratio, and relatively lower fabrication cost. OLEDs possess a multi-layered structure where the emissive layer is sandwiched between electrodes, charge injection and transporting layers. One of the remaining challenges in OLED design is to address the relatively poorer performance of the blue sub pixel compared to the green and red sub pixels. This is because the red and green sub pixels employ phosphorescent complexes while the blue sub pixel relies on a fluorescent organic compound and so exciton harvesting efficiency is inherently lower. There is at present no viable blue phosphorescent complex emitter whose use translates into an OLED with sufficiently high stability.[2–4] Blue light has the highest energy of the three primary display colors, meaning that the emitter must possess the largest bandgap, typically exceeding 2.7 eV. This brings up a challenge as efficient emitters that operate via a thermally activated delayed fluorescence (TADF) mechanism typically rely on an electron donor-acceptor (D-A) molecular structure, which results in a charge transfer (CT) excited state that manifests in broad emission and so does not meet the industry requirement for the blue sub pixel CIE chromaticity coordinates of 0.131, 0.046.[5] Typically, large band gap emitters can be obtained by using a combination of weak electron donors and acceptors; however, the choice of weak acceptors is limited.[6,7] Electron-accepting strength can be quantified by the electron affinity of the compound, which is linked to the energy of the lowest unoccupied molecular orbital (LUMO). One of the most widely explored electron acceptors, 2,4,6-triphenyl-1,3,5-triazine, has LUMO of −1.80 eV (DFT PBE0/6-31G(d,p)) and is considered a relatively strong electron acceptor. Indeed, there are no deep blue TADF emitters that employ this acceptor within the molecular design. Weaker electron acceptors include 1,3,4-oxadiazole (OXD) (LUMO −0.55 eV), pyrimidine (LUMO −1.16 eV), 1,3,4-thiadiazole (LUMO −1.27 eV).[6] Use of stronger donors like 9,9-dimethylacridine (DMAC, HOMO −5.13 eV), phenoxazine (PXZ, HOMO −5.02 eV), or phenothiazine (PTZ, HOMO −5.26 eV) in conjunction with the aforementioned weak acceptors leads to too stabilized singlet excited states for blue emission.[8–15] Often, green emission is observed even when the weak

[a] *Dr. T. Matulaitis, Dr. D. B. Cordes, Prof. A. M. Z. Slawin, Prof. E. Zysman-Colman*
Organic Semiconductor Centre, School of Chemistry,
University of St. Andrews, St. Andrews, Fife,
KY16 9ST, United Kingdom
E-mail: wiley_subscriptions@zysman-colman.com
[b] *Dr. P. L. dos Santos, Prof. I. D. W. Samuel*
Organic Semiconductor Centre, SUPA,
School of Physics and Astronomy, University of St Andrews,
St Andrews, Fife KY16 9SS,
United Kingdom
E-mail: idws@st-andrews.ac.uk
[c] *Dr. P. L. dos Santos*
Current address: Department of Engineering,
Durham University, Durham DH1 3LE
[d] *Dr. Y. Tsuchiya, Prof. C. Adachi*
Center for Organic Photonics and Electronics Research (OPERA),
Kyushu University 744 Motooka, Nishi-ku,
Fukuoka 819-0395, Japan

Supporting information for this article is available on the WWW under https://doi.org/10.1002/slct.202300274

donor carbazole is used in conjunction with these weak acceptors. The resulting emissive CT state is sensitive to the polarity of the surrounding, hence a red-shifted emission is observed.[8,10,11] Deep blue emission is observed only in a handful of reports where a weak acceptor like diphenylsulfone (DPS) (LUMO −1.37 eV) is used with carbazole, or DMAC.[16–18] Other examples of blue emitters involve boron-containing acceptors, such as DOBNA (LUMO −1.50 eV), or other weak acceptors like trifluoromethylated pyridine (LUMO −1.61 eV).[19,20] D-A compounds that are based on these acceptors in conjunction with carbazole and even DMAC show blue TADF; however, it is not possible to obtain blue emission when using stronger donors like PXZ. Here we demonstrate blue emission in donor-acceptor systems bearing strong donors by using an ultra-weak electron-accepting imidazole acceptor.

Imidazole derivatives have been widely explored as both electron-transporting and emitter materials for OLEDs.[21,22] The two nitrogen atoms within the imidazole ring, N1 and N3, possess distinct chemistry and confer bipolar character to the imidiazole with N1 being nucleophilic, while N3 is part of a π-accepting imine (Figure 1a). This N3 nitrogen deepens the LUMO energy of 1,2,4,5-tetraphenylimidazole (**TPI**) to −0.76 eV, which is comparable to that of OXD (−0.55 eV, PBE0/6-31G(d,p)). As well, the LUMO of **TPI** is shallower than those of widely used acceptors in blue TADF emitter design, such as triazine (−1.80 eV), isophthalonitrile (−2.13 eV), or diphenylsulfone (DPS) (−1.37 eV), placing **TPI** as a very weak electron acceptor and a suitable candidate to construct blue emitters.

Various starting precursors can be used in a multi-component condensation reaction to obtain differently substituted imidazole derivatives with structural diversity easily installed at the N1, C2, and C4/5 ring positions. Typical synthesis routes for imidazole-containing emitter materials introduce electron donor, or π-spacer and donor groups at C2.[23–30] These groups tend to be conjugated with the imidazole, as arenes such as phenylene rings adopt a relatively co-planar conformation. By contrast, phenylene substituents at C5 or N1 adopt a significantly more twisted conformation. Most of the reported examples of D-A compounds involving imidazole include a C2-substituted imidazole, these compounds emit either via fluorescence or a hot exciton channel mechanism as the excited state possesses mixed hybridized local and charge-transfer (HLCT) character. There are only a small number of acridine-imidazole derivatives that were reported as thermally activated delayed fluorescent (TADF) emitters (Figure S29, Table S4).[31–33]

In this work we turned our attention to producing D-A compounds functionalized at N1 of the imidazole. To date, there are just a handful examples reported employing donors at the N1 position of imidazole.[21,22,25,34] However, most of these examples also contain substituents at C2 and it is these that dominate the photophysics of the molecule. To study the substituent effect on the imidazole electronics, we designed three new donor-imidazole hybrid materials, 9,9-dimethyl-10-(4-(2,4,5-triphenyl-1H-imidazol-1-yl)phenyl)-9,10-dihydroacridine (**DMAC-TPI**), 10-(4-(2,4,5-triphenyl-1H-imidazol-1-yl)phenyl)-10H-phenoxazine (**PXZ-TPI**), and 10-(4-(2,4,5-triphenyl-1H-imidazol-1-yl)phenyl)-10H-phenothiazine (**PTZ-TPI**), where the donors were connected to tetraphenylimidazole *para* to the N1 phenylene. Density functional theory (DFT) calculations predicted the HOMO to be localized on the donors, while LUMO is localized on the TPI. Time-dependent DFT calculations using Tamm-Dancoff approximation (TDA-DFT)[35] revealed that the singlet-triplet energy gaps, ΔE_{ST}, decrease in the sequence of 0.44 eV, 0.38 eV and 0.19 eV for **PTZ-TPI**, **DMAC-TPI**, and **PXZ-TPI**, respectively, with **PXZ-TPI** being a potential TADF emitter. The optical bandgaps, E^{G}_{opt}, were found to vary from 3.3–3.6 eV, while intramolecular charge transfer (ICT) emission was observed only for **DMAC-TPI** and **PXZ-TPI**. Their steady-state emission was registered (λ_{PL}) at 381 nm and 407 nm in

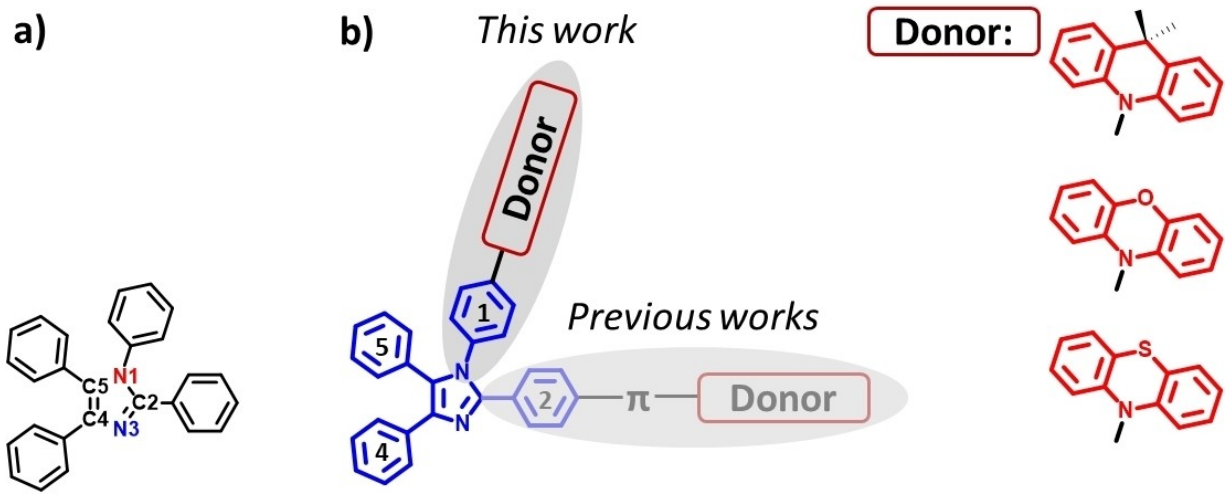

Figure 1. a) Chemical structure of TPI. b) Structural representation of donor-linking pattern used in donor-TPI derivatives.

dilute toluene solutions, respectively. Both compounds were characterised as fluorescent emitters with low photoluminescence quantum yield (Φ_{PL}) values of 9% and 10% in 6 wt% doped films in DPEPO host, and nanosecond fluorescence lifetimes. While the strategy of employing imidazole as a weak electron acceptor in conjunction with strong PXZ electron donor proved to be successful in obtaining deep blue emission, both **DMAC-TPI** and **PXZ-TPI** failed to demonstrate TADF behaviour, primarily due to their too large experimentally observed ΔE_{ST} values (1.22 eV and 1.19 eV, respectively). Connecting a strong donor PTZ group to **TPI** at the N1 position led instead to observation of RTP.

Results and discussion

Synthesis and Chemical Characterization

Tetraphenylimidazole (**TPI**) and 1-(4-bromophenyl)-2,4,5-triphenyl-1H-imidazole (**TPI-Br**) were accessed in high yields in a one-pot four-component condensation reaction under acidic conditions of an aromatic aldehyde, an amine, a dione and ammonium acetate (Scheme 1).[36,37] An attractive feature of this synthesis is that purification involves a recrystallization, obviating the need for column chromatography. Thus, the synthesis is easily scalable at low cost. Target materials 9,9-dimethyl-10-(4-(2,4,5-triphenyl-1*H*-imidazol-1-yl)phenyl)-9,10-dihydroacridine (**DMAC-TPI**), 10-(4-(2,4,5-triphenyl-1*H*-imidazol-1-yl)phenyl)-10*H*-phenoxazine (**PXZ-TPI**), and 10-(4-(2,4,5-triphenyl-1*H*-imidazol-1-yl)phenyl)-10*H*-phenothiazine (**PTZ-TPI**) were obtained via Buchwald-Hartwig animation[38] of **TPI-Br** with either dimethylacridan (DMAC), phenoxazine (PXZ), or phenothiazine (PTZ), respectively. All the target materials were obtained in relatively high yields. The identity and purity of the compounds were confirmed by ^{1}H and ^{13}C NMR spectroscopy, high-resolution mass spectrometry, melting point determination and elemental analysis. **DMAC-TPI**, **PXZ-TPI**, and **PTZ-TPI** were found to be thermally stable with their decomposition temperatures (T_D) at which 5% loss of mass is registered exceeded 370 °C.

Crystal structure of TPI and PTZ-TPI

Single crystals suitable for X-ray diffraction of **TPI** were obtained by diffusion of acetone into a dichloromethane solution of **TPI** (Figure 2). The structure of **TPI** is similar to the version that has been determined previously,[39] despite a higher-symmetry space group and resulting symmetry-induced disorder in the structure. The symmetry-related phenyl groups on C2 and C4 adopt a shallow inclination relative to the plane of the imidazole (interplanar angle 25.51°), while those on N1 and C5 are closer to orthogonal (72.56° between planes. Differences in the relative interplanar angles lead to differences in packing; all molecules packing with the imidazole plane lying parallel to the (1 0 1) plane, in contrast to the known

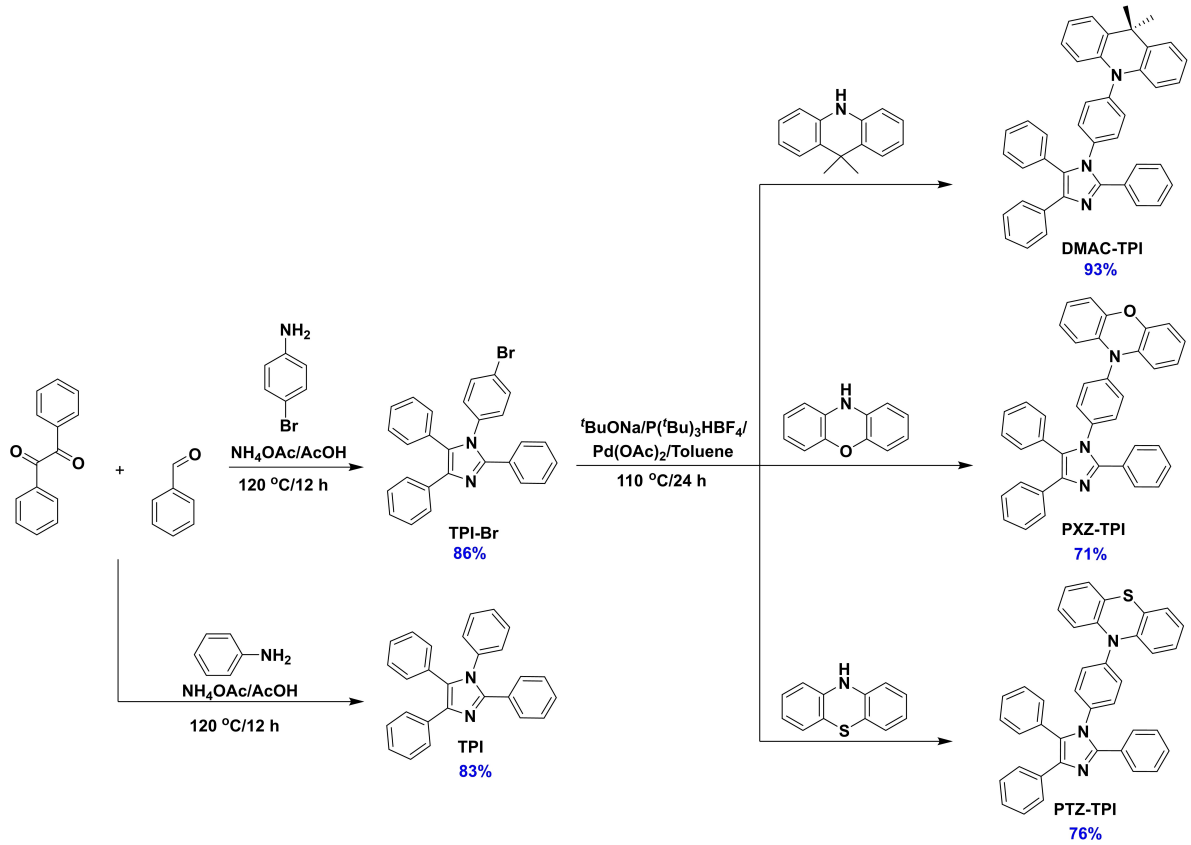

Scheme 1. Synthesis of TPI derivatives.

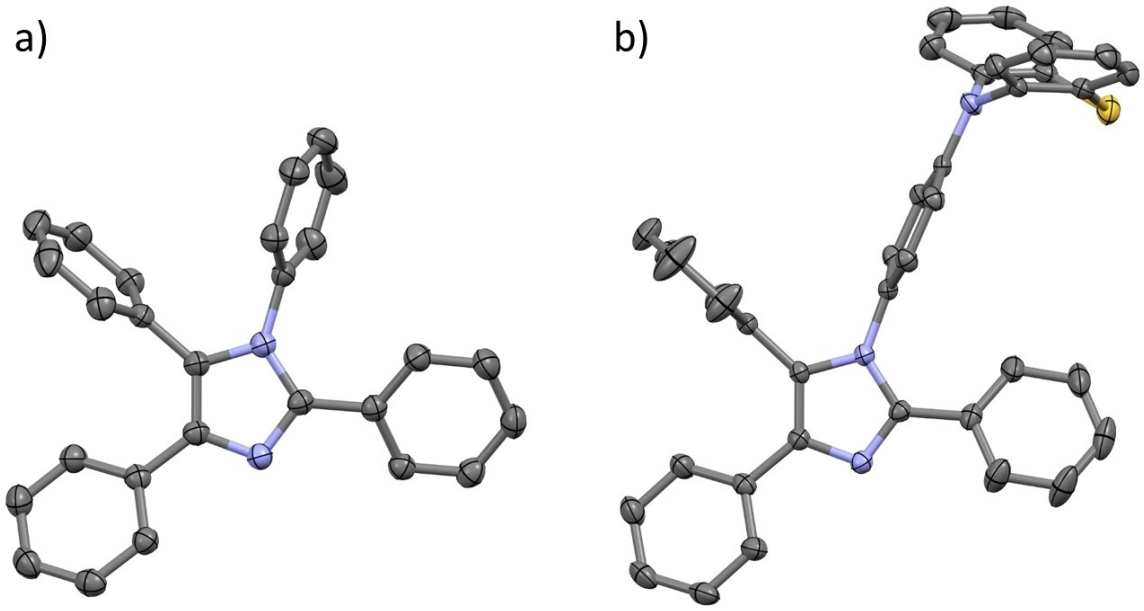

Figure 2. Thermal ellipsoid plots (50% probability ellipsoids) of the crystal structures of a) **TPI** and b) **PTZ-TPI**. Hydrogens are omitted for clarity and only one component of symmetry-induced disorder in **TPI** is shown.

structures where half of the molecules are oriented parallel to (1 0 1) and half parallel to (0 1 1).

Single crystals suitable for X-ray diffraction of **PTZ-TPI** were obtained directly from temperature gradient sublimation (Figure 2). The most notable feature found in the structure was that the PTZ adopts an axial conformation with an C9-N12-S19 angle of 111.68°. The PTZ shows a butterfly geometry, with the angles between its aromatic ring planes being 44.47°. TPI adopts a twisted conformation where the phenyl groups 1 and 5 being nearly orthogonal to the imidazole plane (83.62 and 89.79° between planes). By contrast, the phenyl groups 2 and 4 were found to be close to the same plane as the imidazole (18.88 and 22.43° between planes). Weak intermolecular C–H···π interactions were found between the neighboring molecules with H···centroid distances being 2.76 and 2.80 Å [corresponding C···centroid distances of 3.4477(17) and 3.5426(18) Å].

Theoretical Calculations

Density Functional Theory (DFT) calculations at the PBE0/6-31G(d,p) level[40,41] were performed to gain insight of the optoelectronic properties of the studied materials. The nature of the excited singlet and triplet states and their energies were determined from time-dependent density functional theory (TD-DFT) within the Tamm-Dancoff approximation (TDA)[35,42] at the same level of theory. The TPI core adopts a geometry in the ground state where all four phenyl rings are twisted with respect to the plane of the imidazole: phenyl rings 1 and 5 are twisted by 68° and 51°, respectively, while phenyl groups 2 and 4 are twisted by 29° and 25°, respectively (Figure 3a). The dihedral angle between the phenylene bridge and the **TPI** core decreases by 6–7° in the donor-acceptor compounds, while the donor groups are themselves disposed in a close-to perpendicular orientation with respect to the bridge. DMAC was found to adopt the most twisted conformation, followed by PTZ and PXZ with torsion angles of 83°, 81°, and 71°, respectively (Figure 3b–d). Such a high degree of twisting is expected to lead to only minimal conjugation between the donor and the rest of the molecule. Calculated HOMO, LUMO, S_1 and T_1 energies, as well as HOMO and LUMO topologies of **TPI**, **DMAC-TPI**, **PXZ-TPI**, and **PTZ-TPI** are shown in Figure 4. While in **TPI** local excitations occur over the entire compound, introduction of the poorly electronically coupled donors results in charge separation. The HOMOs of **DMAC-TPI**, **PXZ-TPI**, and **PTZ-TPI** are mostly localized over the DMAC, PXZ and PTZ, respectively, with a small portion of electron density residing on the phenylene spacer. **TPI** acts as the electron acceptor in these systems as the LUMOs were found to be delocalized throughout the imidazole core with all the adjascent phenylenes involved; phenyl group 4 contributes less to the electron density distribution of the LUMOs of these compounds than the other phenyl groups. The HOMO level of **TPI** is −5.45 eV (−5.46 eV,[43] calculated using B3LYP functional). Introduction of the donors results in a destabilization of the HOMO by 9–42 meV. The relative HOMO levels of **DMAC-TPI**, **PXZ-TPI**, and **PTZ-TPI** at −5.28, −5.03 and −5.36 eV, respectively, reveal that in this family of compounds the donor strength increases from PTZ to DMAC to PXZ. The LUMO level of **TPI** is −0.76 eV, which classifies this moiety as a weak electron acceptor. We note that there is discrepancy with previously reported calculated LUMO value for **TPI** of −1.16 eV,[43] however, this value was obtained using B3LYP functional, while we used PBE0 instead. The increased conjugation in the donor-acceptor compounds leads

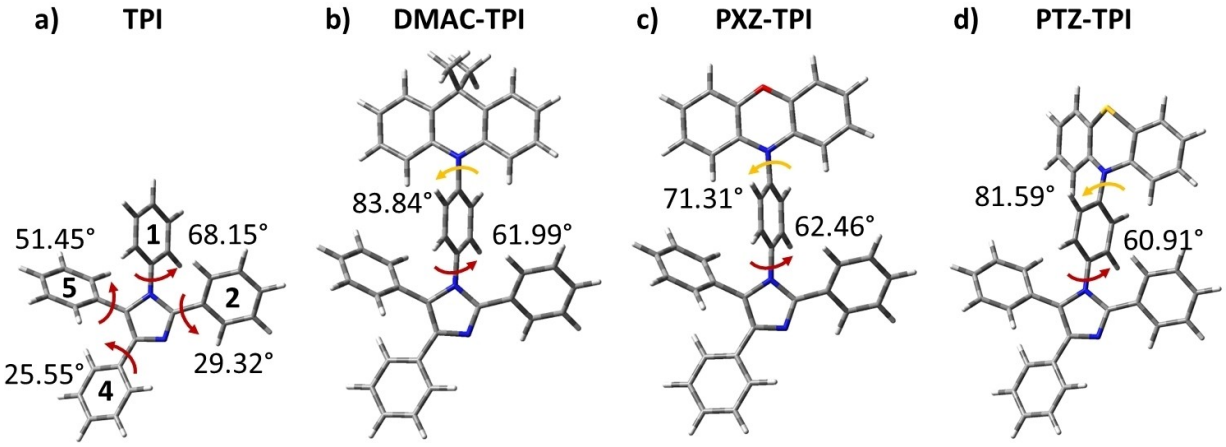

Figure 3. Optimized ground state geometries in the gas phase at the PBE0/6-31G(d,p) level of theory of a) **TPI**, b) **DMAC-TPI**, c) **PXZ-TPI** and d) **PTZ-TPI**.

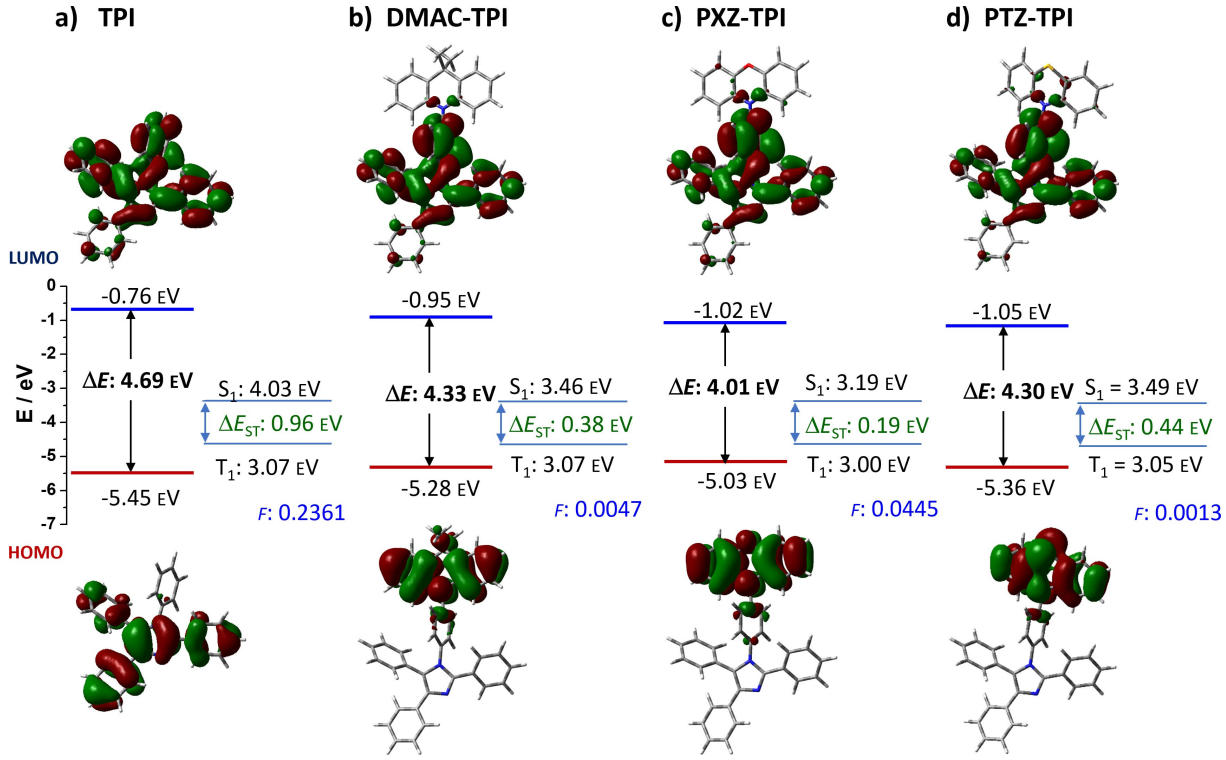

Figure 4. DFT calculated HOMO, LUMO, S_1 and T_1 energies, as well as HOMO and LUMO topologies (isovalue = 0.02) of a) **TPI**, b) **DMAC-TPI**, c) **PXZ-TPI** and d) **PTZ-TPI** (isovalue = 0.02) at the PBE0/6-31G(d,p) level in vacuum.

to a stabilized LUMO, with shallow values of −0.95, −1.02 and −1.05 eV for **DMAC-TPI**, **PXZ-TPI**, and **PTZ-TPI**, respectively.

Both the singlet and triplet energies of **TPI** (E_{S1} = 4.03 eV, E_{T1} = 3.07 eV) are very high. Notably, the incorporation of donors *para*- to the N1-phenylene of imidazole do not appreciably stabilize the T_1 state of the corresponding molecules, reflecting a common triplet state of locally excited (LE) character across the three compounds. In **DMAC-TPI**, TDA-DFT calculations predicted that the dominant transition to the T_1 state to be LE in nature (HOMO-1→LUMO, 67%), localized on the TPI moiety (Figure S22). Similarly, the T_1 of **PTZ-TPI** (HOMO-1→LUMO, 0.58%) is LE on TPI, while in case of **PXZ-TPI** the nature of T_1 is now localized on the PTZ donor, with the principal transition now HOMO→LUMO + 4 (61%) (Figure S22). The TDA-DFT computed T_1 energies of **DMAC-TPI**, **PXZ-TPI**, and **PTZ-TPI** are 3.07, 3.00 and 3.05 eV, respectively. The S_1 states of the three donor-acceptor compounds, however, are stabilized and adopt significant charge transfer (CT) character. This results in much smaller singlet-triplet gaps. Indeed, ΔE_{ST} values decreased from 0.96 eV for **TPI** to 0.44, 0.38 and 0.19 eV for

PTZ-TPI, **DMAC-TPI** and **PXZ-TPI**, respectively, in line with the increasing strength of the donor. The oscillator strength (*f*) for the transition to the S_1 state of **TPI** is typically large at $2.36 \cdot 10^{-1}$ for a state with LE character. The *f* for **DMAC-TPI**, and **PTZ-TPI** indicate weak orbital overlap with values of $4.7 \cdot 10^{-3}$, $1.3 \cdot 10^{-3}$, respectively. **PXZ-TPI**, on the other hand, shows a much larger *f* of $4.4 \cdot 10^{-2}$, reflective of the increased orbital overlap desipte the smallest ΔE_{ST} in this family of compounds, making it the most promising candidate as an effective TADF emitter. We have also optimized the T_1 state geometries of these molecules (see Figure S22). DFT predicted **DMAC-TPI** and **PTZ-TPI** to retain the triplet spin density localised over TPI moiety. **PXZ-TPI** experiences more changes in its geometry, resulting in triplet spin density delocalised over the whole molecule.

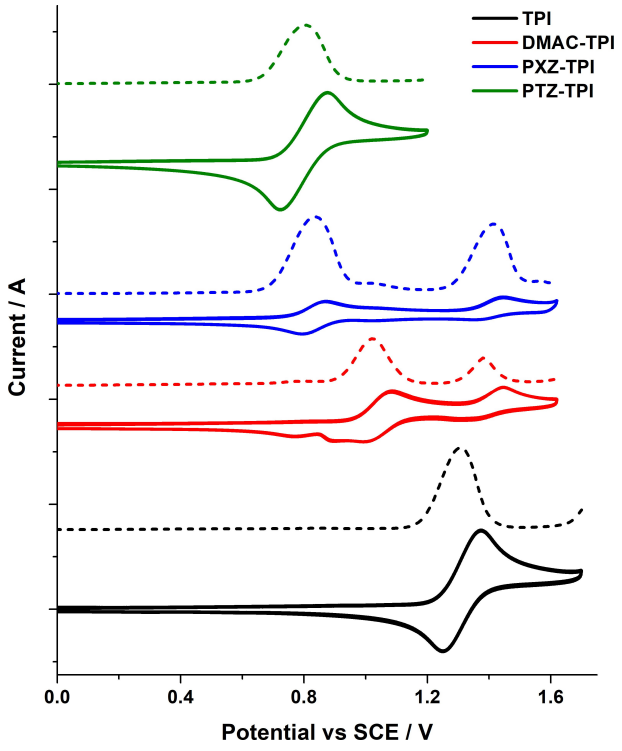

Figure 5. CVs and DPVs of **TPI**, **DMAC-TPI** and **PXZ-TPI**. in DCM, reported versus SCE ($Fc/Fc^+ = 0.34$ V in DCM,[44] scan rate = 100 mV s^{-1}).

Electrochemistry

Electrochemical properties were studied by cyclic voltammetry (CV) and differential pulse voltammetry (DPV) in DCM and the resulting voltammograms are shown in Figure 5 while the summary of electrochemical properties is found in Table 1. Upon scanning anodically, **TPI** undergoes a reversible oxidation at 1.08 V ($E^{OX}_{1/2}$). Previously **TPI** oxidation was reported at 1.54 V (E^{OX}_{onset}) in DMF.[43] With the introduction of donor groups, a new, cathodically shifted oxidation wave appears at 0.80 V and 0.62 V for **DMAC-TPI** and **PXZ-TPI**, corresponding to the oxidation of the DMAC and PXZ donors, respectively, the former being pseudo-reversible while the latter being reversible. The TPI-centred oxidation anodically shifts to 1.16 V and 1.17 V, becoming less reversible. In case of **PTZ-TPI** no TPI-centred oxidation is observed, instead a new oxidation wave registered at 0.85 V ($E^{OX}_{1/2}$). The corresponding ionization potentials (IP) for **TPI**, **DMAC-TPI**, **PXZ-TPI**, and **PTZ-TPI** are 6.08 eV, 5.80 eV, 5.62 eV, and 5.61 eV, respectively. No reduction waves were observed within the electrochemical window, revealing the weak electron-accepting nature of the TPI. Therefore, the electron affinities (EA) were estimated using optical bandgaps at 2.45 eV, 2.24 eV, 2.31 eV, and 2.06 eV for **TPI**, **DMAC-TPI**, **PXZ-TPI**, and **PTZ-TPI**, respectively. The inclusion of the donor groups resulted in a destabilization of the LUMO and a decrease in the EA value of TPI by ca. 0.2 eV, a trend that is captured by DFT where the LUMO energies were destabilized by ca. 0.2–0.3 eV with donor introduction.

Photophysical Characterization

UV/Visible absorption spectra were recorded in 10^{-5} M toluene solutions and are shown in Figure 6a. **TPI** shows a single absorption band located at λ_{abs} 291 nm ($\varepsilon = 36 \times 10^3$ M^{-1} cm^{-1}). DFT predicts this state to be a locally excited (LE) state (Figure S23). All compounds showed no new features but did exhibit slight broadening of the characteristic TPI absorption band. The absorption spectrum of **DMAC-TPI** resembles that of **TPI**, with slightly increased molar absorption at 291 nm ($\varepsilon = 46 \times 10^3$ M^{-1} cm^{-1}). DFT predicted S_1 state of ICT nature at 358 nm with low oscillator strength (*f*) value of 4.8×10^{-3}. This was not observed in the experiment but would have been too weak to detect. Introduction of the stronger donors PTZ and

Table 1. Summary of optical and electrochemical properties.

	E^G_{opt} /eV[c]	λ_{PL} (FWHM)/nm[b]		λ_{PL} (FWHM)/nm[c]		E_{S1}/eV[d]	E_{T1}/eV[d]	ΔE_{ST}/eV[d]	Φ_{PL}[e]	$E^{OX}_{1/2}$/V *vs* SCE[f]	IP/eV[f]	EA/eV[g]
TPI	3.63	382	(64)	362	(46)	4.00	2.75	1.25	0.52	1.08	6.08	2.45
DMAC-TPI	3.56	388	(56)	381	(50)	3.96	2.74	1.22	0.10	0.80	5. 80	2.24
PXZ-TPI	3.31	418	(63)	407	(60)	3.97	2.79	1.19	0.09	0.62	5.62	2.31
PTZ-TPI	3.55	443	(69)	508	(96)	3.23	2.61	0.62	–*	0.85	5.61	2.06

(a) Optical bandgap was determined from the absorption and emission intersection using formula $E^G_{opt} = \frac{1240}{\lambda}$ eV in toluene. (b) Measured in toluene at room temperature. λ_{PL} is the photoluminescence peak maximum, FWHM is the full width at half maximum. $\lambda_{exc} = 320$ nm. (c) Measured in Zeonex (1 wt%) at room temperature. $\lambda_{exc} = 320$ nm. (d) Singlet and triplet energies were estimated from the respective onsets of prompt and phosphorescence emissions in toluene glass at 77 K. (e) Photoluminescence quantum yields (Φ_{PL}) of 6 wt.% **TPI**, **DMAC-TPI** and **PXZ-TPI** doped in DPEPO. *Φ_{PL} of **PTZ-TPI** was not determined. (f) Oxidation potentials ($E^{OX}_{1/2}$) were estimated from DPV in DCM. Values are versus SCE ($Fc/Fc^+ = 0.46$ V in DCM[45]), scan rate 50 mV/s. (e) $IP = -(E^{OX}_{1/2\ vs\ Fc/Fc+} + 4.8)$[46] eV. (g) Electron affinities were estimated using formula $EA = |IP - E^G_{opt}|$

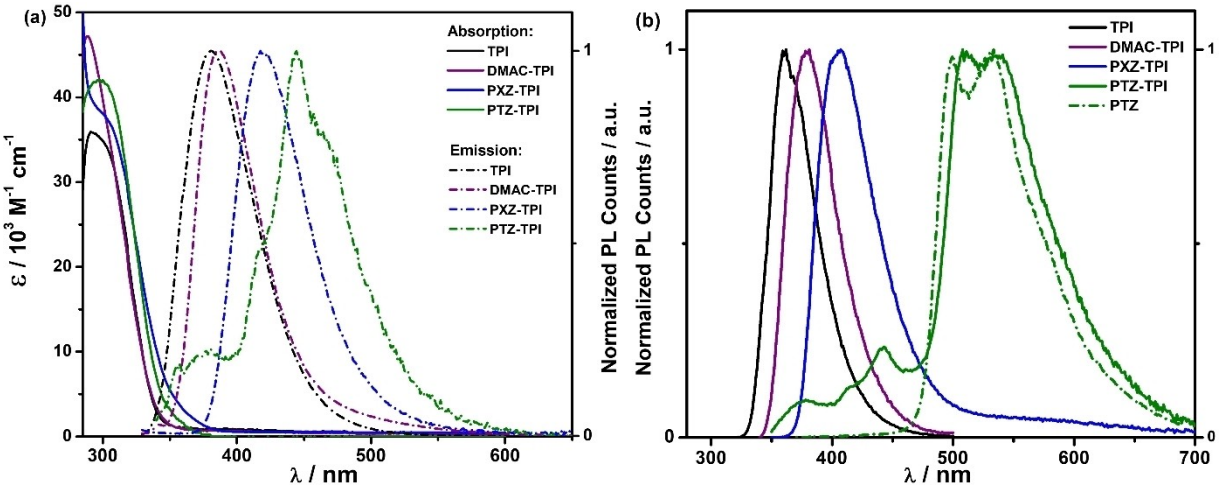

Figure 6. (a) UV/Vis absorption and steady-state photoluminescence spectra of **TPI**, **DMAC-TPI**, **PXZ-TPI** and **PTZ-TPI** in toluene (10^{-5} M concentration, $\lambda_{exc} = 300$ nm) and (b) photoluminescence spectra in Zeonex (1 wt. %) at room temperature. Phosphorescence spectrum of dilute phenothiazine 10^{-5} M solution in toluene at 77K is also included (green dotted line, $\lambda_{exc} = 355$ nm).

PXZ to **TPI** resulted in further broadening of the main LE absorption band and again, only a slight increase in molar absorptivity at 291 nm ($\varepsilon_{PXZ\text{-}TPI} = 40\times10^3\ M^{-1}cm^{-1}$ and $\varepsilon_{PTZ\text{-}TPI} = 41\times10^3\ M^{-1}cm^{-1}$) with **PXZ-TPI** showing the most red-shifted absorption. The low intensity tail located at 350–380 nm ($\varepsilon = 2.4\times10^3\ M^{-1}cm^{-1}$ at 365 nm) is ascribed to an ICT transition occurring within **PXZ-TPI**, as shown by DFT with a S_1 state mainly composed of HOMO→LUMO transition occurring at 388 nm with $f = 4.45\times10^{-2}$. The very low intensity of the HOMO→LUMO transition in **PTZ-TPI** (S_1, $f = 1.3\times10^{-3}$) is likely responsible for lack of this absorption band in the experiment.

TPI emits at λ_{PL} of 382 nm with full width at half maximum (FWHM) of 0.51 eV (64 nm) in toluene (Figure 6a). The emission spectrum of **DMAC-TPI** is slightly narrower and the peak is only 6 nm (0.05 eV) red-shifted compared to that of **TPI**, which is an indication that upon photoexcitation at 300 nm, emission from a TPI-based LE state dominates in both compounds. The emission spectrum of **PXZ-TPI** is 36 nm (0.28 eV) red-shifted compared to that of **TPI** however, both **DMAC-TPI** and **PXZ-TPI** emission spectra show the same FWHM of 0.44 eV (63 nm) and 0.42 eV (64 nm), respectively, indicating just a weakly extended conjugation in the chromophore (**TPI**), rather than occurrence of typical broad intramolecular charge transfer (ICT) band. **PTZ-TPI** showed dual-luminescence, originating from LE emission from each of **TPI** and **PTZ** in this compound (Figure S24). Apparently, in this compound both chromophores are photo-excited simultaneously and there is no observable ICT emission. Changing the polarity of the solvent did not have any impact on the shape and position of **TPI** emission, while the emission spectra of both **DMAC-TPI** and **PXZ-TPI** showed modest positive solvatochromism (Figure S25). For **PTZ-TPI**, moving to more polar solvents resulted only in relatively higher contribution from the TPI emission to the overall PL, and no ICT emission band was detected.

We next investigated the photophysical behavior in the solid-state (Figure 6b). The emission spectra of 1 wt% doped **TPI**, **DMAC-TPI** and **PXZ-TPI** films in Zeonex are blue-shifted and narrower than those in solution. Zeonex is a nonpolar polymer host, thus the observed blue-shift and narrowing in **DMAC-TPI** and **PXZ-TPI** emission is expected based on its relative polarity compared to toluene. In the case of **TPI** this blue-shift can be attributed to suppression of non-radiative decay channels in the solid state as compared to the solution. **PXZ-TPI** shows a low intensity red-shoulder in its PL spectrum, likely the result of excimer emission (Figure 6b). Finally, room temperature phosphorescence (RTP) originating from **PTZ** was observed in **PTZ-TPI**. This RTP was accompanied by simultaneous emission from the S_1 states of both **TPI** and **PTZ** (see Figure S24 for band assignments). Occurrence of such multiple emission processes indicate that there is no electronic communication between **TPI** and **PTZ** in the excited state of **PTZ-TPI**. Next, the compounds under investigation were co-doped with the high triplet-energy host bis[2-(diphenylphosphino)phenyl]ether oxide (DPEPO). Note that as **PTZ-TPI** showed no ICT emission and thus is not a candidate TADF material, no further investigation to its photophysical properties in DPEPO was pursued. A doping concentration of 6 wt% was found to be an optimal (Table S2 and Figure S26) in terms of photoluminescence quantum yields. Both **DMAC-TPI** and **PXZ-TPI** demonstrated PLQY values not exceeding 10%, this due in part to the very low oscillator strength for the low-energy transitions. More importantly, emission broadening and the appearance of a red shoulder in the PL spectra of **DMAC-TPI** and **PXZ-TPI** were observed. This new emissive band increased in intensity with increasing doping concentration. Based on IP/EA values of these compounds, this new band cannot be the result of an exciplex between the host and emitter; thus, these red shoulders may arise from excimer/aggregate species. The emission of **TPI**, **DMAC-TPI** and **PXZ-TPI**

in DPEPO decays with nanosecond-long lifetimes, no delayed component was observed (Figure S27).

Figure 7 shows the prompt fluorescence and phosphorescence spectra of **TPI**, **DMAC-TPI**, **PXZ-TPI** and **PTZ-TPI** in toluene glass at 77 K. S_1 and T_1 energies of **TPI** were determined at 4.00 eV and 2.75 eV, respectively, and the singlet-triplet energy splitting (ΔE_{ST}) at 1.25 eV (Table S3). Prompt emission and phosphorescence of **DMAC-TPI** resembled those of **TPI**, with only slightly altered S_1 and T_1 levels. The prompt emission peak of **PXZ-TPI** resembles that of **TPI** at an energy of 3.97 eV. A complex emission profile is observed in the phosphorescence spectrum of **PXZ-TPI**. Superimposing **PXZ-TPI** phosphorescence with those of TPI and PXZ allowed us to ascribe individual bands to each of the chromophores (Figure S28). The blue bands at 2.79 eV are associated with phosphorescence of PXZ, while the red onset matches that of TPI. The increase in triplet energy compared to **TPI**, however, was not sufficient to reduce the ΔE_{ST} to enable TADF in **PXZ-TPI** (1.19 eV). We note that the gas phase TDA-DFT computed ΔE_{ST} values for **DMAC-TPI** and **PXZ-TPI** (0.38 and 0.19 eV, respectively) are much smaller than the experimentally determined single-triplet gaps, possibly because the calculation predicts CT singlet excited states, whereas we observe LE-type behaviour for the prompt emission (for a wider discussion of the DFT results, see ESI). Nevertheless, the TDA-DFT calculations did predict the nature of the T_1 states correctly, with T_1 state of **DMAC-TPI** being localised on **TPI**, while that of **PXZ-TPI** being of mixed CT/LE character. **PTZ-TPI** showed very weak fluorescence yet intense phosphorescence in frozen toluene matrix at 77 K. This phosphorescence is dominated by triplet emission from PTZ, as the spectrum aligns with that of PTZ in Zeonex at room temperature (Figure 6b, S24). The ΔE_{ST} of **PTZ-TPI** is thus of a similar magnitude to that of PTZ (0.62 eV vs 0.53 eV) and is significantly smaller than in the other two compounds (each at ~1.2 eV). As both the singlet and triplet excited states are localized on the PTZ, spin-orbit coupling is not possible according to El Sayed's rule and thus no exciton upconversion is likely to occur.

Conclusions

We have synthesized three new tetraphenylimidazole derivatives bearing electron donors of different strength. The donors were connected to imidazole via the N1 phenylene. Compounds were accessed via a 2-step synthetic route from inexpensive starting materials. Photophysical investigation revealed a lack of charge transfer character in the N1 donor-substituted imidazoles. Only **PXZ-TPI** showed CT emission in polar DCM, however, dual prompt emission and dual phosphorescence was observed at low temperature indicating that in this compound chromophores are also decoupled in the excited state, favouring the locally excited state emission.

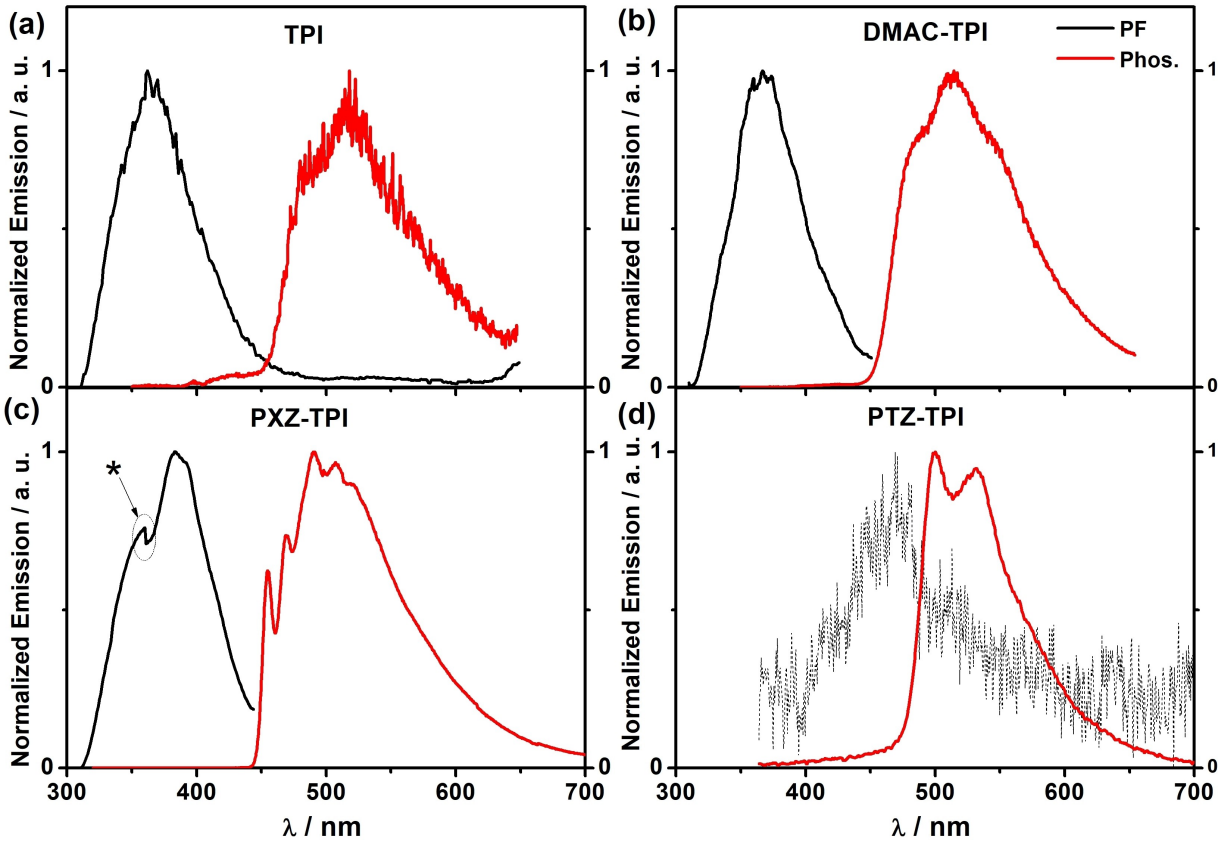

Figure 7. Prompt fluorescence and phosphorescence spectra of a) **TPI**, b) **DMAC-TPI**, c) **PXZ-TPI** and d) **PTZ-TPI** 10^{-5} M in toluene at 77 K. $\lambda_{exc} = 310$ nm, * instrument artefact.

Similar properties were observed for the compound **PTZ-TPI**, bearing the even stronger electron donor PTZ. This compound demonstrated only LE emission originating from TPI and PTZ in all the investigated media. In the solid state, room temperature phosphorescence from PTZ was observed. Our study showed that TPI coupled with donors via N1 position is too weak an electron acceptor to enable ICT, and hence TADF does not occur. Instead, such a design can potentially be used in RTP-active compound design.

Experimental section

All reagents and solvents were obtained from commercial sources and used as received. Air-sensitive reactions were performed under a nitrogen atmosphere using Schlenk techniques, no special precautions were taken to exclude air or moisture during work-up and crystallisation. Anhydrous toluene was obtained from a Pure Solv™ solvent purification system (Innovative Technologies). Flash column chromatography was carried out using silica gel (Silia-P from Silicycle, 60 Å, 40–63 μm). Analytical thin-layer-chromatography (TLC) was performed with silica plates with aluminum backings (250 μm with F-254 indicator). TLC visualization was accomplished by 254/365 nm UV lamp. HPLC analysis was conducted on a Shimadzu Prominence Modular HPLC system. HPLC traces were performed using an ACE Excel 2 C18 analytical column. ^{1}H and ^{13}C NMR spectra were recorded on a Bruker Advance spectrometer (Larmor frequencies of 400 MHz and 101 MHz or 500 MHz and 126 MHz, respectively). Melting points were measured using open-ended capillaries on an Electrothermal melting point apparatus IA9200 and are uncorrected.

High-resolution mass spectrometry (HRMS) was performed by EPSRC National Mass Spectrometry Service Centre (NMSSC), Swansea. Elemental analyses were performed at the School of Geosciences at the University of Edinburgh. X-ray diffraction data for both compounds were collected at 173 K using a Rigaku FR–X Ultrahigh Brilliance Microfocus RA generator/confocal optics with XtaLAB P200 diffractometer [Mo Kα radiation (λ = 0.71073 Å)]. Intensity data were collected using ω steps accumulating area detector images spanning at least a hemisphere of reciprocal space. Data for all compounds analysed were collected using CrystalClear[47] and processed (including correction for Lorentz, polarization and absorption) using CrysAlisPro.[48] The structures were solved by direct methods (SIR2011[49]) and refined by full-matrix least-squares against F^2 (SHELXL-2018/3[50]). Non-hydrogen atoms were refined anisotropically, and hydrogen atoms were refined using a riding model. All calculations were performed using the Olex2[51] interface. Selected crystallographic data are presented in Table S1. CCDC 2219099-2219100 contains the supplementary crystallographic data for this paper. These data can be obtained free of charge from The Cambridge Crystallographic Data Centre via www.ccdc.cam.ac.uk/structures.

Ground-state gas phase optimizations were carried out using Density Functional Theory (DFT) employing the PBE0 functional with the Pople 6-31G(d,p)[52] basis set, followed by a frequency calculation for each compound to ensure that an energy minimum was reached. Excited-state calculations were performed employing the Tamm-Dancoff approximation (TDA)[53,54] to Time-Dependent DFT (TD-DFT) using the same functional and basis set for ground state geometry optimization. Gaussian09[55] software was employed for the calculations, while the results were visualised using GaussView[56] and GaussSum[57] software. The singlet-triplet splitting energy $\triangle E_{ST}$ was estimated following the literature methodology.[58] Vertical excitation energy values from the ground state (S_0) to the first lowest singlet- (E_{S1}) and triplet-excited state (E_{T1}) were obtained from TDA-DFT calculations based on optimized ground state geometry and $\triangle E_{ST}$ is then determined using equation: $\triangle E_{ST} = E_{S1} - E_{T1}$.

Cyclic Voltammetry (CV) analysis was performed on an Electrochemical Analyzer potentiostat model 620E from CH Instruments at a sweep rate of 100 mV/s. Differential pulse voltammetry (DPV) was conducted with an increment potential of 0.004 V and a pulse amplitude, width, and period of 50 mV, 0.06, and 0.5 s, respectively. Samples were prepared as dichloromethane (DCM) solutions, which were degassed by sparging with DCM-saturated nitrogen gas for 15 minutes prior to measurements. All measurements were performed using 0.1 M DCM solution of tetra-*n*-butylammonium hexafluorophosphate ([^{n}Bu$_4$N]PF$_6$]). An Ag/Ag$^+$ electrode was used as the reference electrode while a platinum electrode and a platinum wire were used as the working electrode and counter electrode, respectively. The redox potentials are reported relative to a saturated calomel electrode (SCE) with a ferrocenium/ferrocene (Fc/Fc$^+$) redox couple as the internal standard (0.46 V vs SCE).[59]

Three types of samples were studied in this work: i) solution, ii) spin-coated films and iii) evaporated films. i) Optically dilute solutions of concentrations on the order of 10^{-5} were prepared in HPLC grade toluene, *N,N*-dimethylformamide (DMF) and DCM; ii) Spin-coated films were produced from chloroform solutions of blends (10 wt% guest to host) at 2000 rpm for 60 seconds; iii) Evaporated films (10 % wt) were thermally evaporated onto fused silica substrates using an EcoVac evaporator system (Angstrom Engineering, Inc.) at 10^{-7} mbar with a final thickness ~150 nm. Absorption spectra of solutions were recorded at room temperature on a Shimadzu UV-1800 double beam spectrophotometer with a 1 cm fused silica cuvette. Molar absorptivity values were determined from at least five independent solutions at varying concentrations with absorbance ranging from 1.16×10^{-5} to 8.69×10^{-6} M.

Steady-state emission spectra and time-resolved decay curves were recorded for solutions and spin coating films using two spectrofluorometers: an Edinburgh Instruments F980 and a multichannel spectrofluorometer (FP-8600, JASCO). The photoluminescence quantum yield, Φ_{PL}, of solutions was measured using an absolute photoluminescence quantum yield measurement system (C13534-21, Hamamatsu Photonics) under the flow of argon gas with an excitation wavelength of 340 nm, while the Φ_{PL} of evaporated films was measured using an integrating sphere in a Hamamatsu C9920-02 system[60] with excitation at 300 nm under air and under constant nitrogen gas flow. The transient photoluminescence decay curves were obtained under Ar flow using a fluorescence lifetime spectrometer (C11367, Hamamatsu Photonics). The steady-state spectra were recorded at room temperature using excitations at 300 nm, 340 nm (Xenon lamp) while the time-resolved decay curves were recorded at several temperatures (77 K, 200 K, 250 K and 300 K) with excitation at 280 nm and 378 nm (PDL 800-D pulsed diode laser). Time-resolved decay curves for prompt fluorescence (100 ns time window) were recorded using time correlated single photon counting (TCSPC) while time-resolved decay curves for delayed fluorescence (1 ms time window) were recorded using multi-channel scaling (MCS). Time-resolved spectra (phosphorescence) were obtained on evaporated films using a gated intensified charge coupled device (iCCD camera) from

Stanford Computer Optics at 77 K and under laser excitation at 343 nm (100 Hz).

Supporting Information

Instrument details, synthetic procedures, and chemical characterization (NMR spectra, HRMS spectra, elemental analysis reports, HPLC chromatograms), computational details, photophysical characterization and details of X-ray crystallography are available in the Supporting Information file1. The xyz coordinates corresponding to the ground state optimized geometries of **TPI**, **DMAC-TPI**, **PXZ-TPI**, and **PTZ-TPI** are available in Supporting Information file 2.

Acknowledgements

The St Andrews team is grateful to the Engineering and Physical Sciences Research Council (EPSRC) for support from grants EP/P010482/1, EP/R035164/1 and EP/L017008. The St Andrews team is also grateful to Changfeng Si, who has kindly provided the DMAC donor for the synthesis, as well as to Joydip De, who has kindly measured the thermal properties. Kyushu team would like to acknowledge Kyulux inc and JSPS Core-to-Core Program (grant number: JPJSCCA20180005) for the support of this project.

Conflict of Interest

The authors declare no conflict of interest.

Data Availability Statement

The research data supporting this publication can be accessed at https://doi.org/10.17630/2a75f75c-f023-4c2b-a06d-5ed67454c81b

Keywords: Bipolar · charge transfer · DFT · photophysics · weak acceptor

[1] DSCC, "Quarterly OLED Shipment Report," can be found under https://www.displaysupplychain.com/report/quarterly-oled-shipment-report, **2022**.
[2] H. J. Jang, J. Y. Lee, J. Kim, J. Kwak, J.-H. Park, *J. Inf. Disp.* **2020**, *21*, 1–9.
[3] J.-H. Lee, C.-H. Chen, P.-H. Lee, H.-Y. Lin, M. Leung, T.-L. Chiu, C.-F. Lin, *J. Mater. Chem. C* **2019**, *7*, 5874–5888.
[4] A. K. Pal, S. Krotkus, M. Fontani, C. F. R. Mackenzie, D. B. Cordes, A. M. Z. Slawin, I. D. W. Samuel, E. Zysman-Colman, *Adv. Mater.* **2018**, *30*, 1804231.
[5] "BT.2020: Parameter values for ultra-high definition television systems for production and international programme exchange," can be found under https://www.itu.int/rec/R-REC-BT.2020-2-201510-I/en, **2015**.
[6] Y. Im, M. Kim, Y. J. Cho, J.-A. Seo, K. S. Yook, J. Y. Lee, *Chem. Mater.* **2017**, *29*, 1946–1963.
[7] Y. Tsuchiya, K. Tsuji, K. Inada, F. Bencheikh, Y. Geng, H. S. Kwak, T. J. L. Mustard, M. D. Halls, H. Nakanotani, C. Adachi, *Front. Chem.* **2020**, *8*, 403.
[8] Y. J. Cho, S. K. Jeon, B. D. Chin, E. Yu, J. Y. Lee, *Angew. Chem. Int. Ed.* **2015**, *54*, 5201–5204; *Angew. Chem.* **2015**, *127*, 5290–5293.
[9] Y. K. Chen, J. Jayakumar, C. M. Hsieh, T. L. Wu, C. C. Liao, J. Pandidurai, C. L. Ko, W. Y. Hung, C. H. Cheng, *Adv. Mater.* **2021**, *33*, 2008032.
[10] X. Lv, Y. Wang, N. Li, X. Cao, G. Xie, H. Huang, C. Zhong, L. Wang, C. Yang, *Chem. Eng. J.* **2020**, *402*, 126173.
[11] H. J. Lee, H. L. Lee, S. H. Han, J. Y. Lee, *Chem. Eng. J.* **2022**, *427*, 130988.
[12] H. L. Lee, K. H. Lee, J. Y. Lee, H. J. Lee, *J. Mater. Chem. C* **2021**, *9*, 7328–7335.
[13] H. Tanaka, K. Shizu, H. Miyazaki, C. Adachi, *Chem. Commun.* **2012**, *48*, 11392–11394.
[14] X. Wang, J. Hu, J. Lv, Q. Yang, H. Tian, S. Shao, L. Wang, X. Jing, F. Wang, *Angew. Chem. Int. Ed.* **2021**, *60*, 16585–16593; *Angew. Chem.* **2021**, *133*, 16721–16729.
[15] H. Uoyama, K. Goushi, K. Shizu, H. Nomura, C. Adachi, *Nature* **2012**, *492*, 234–238.
[16] Q. Zhang, J. Li, K. Shizu, S. Huang, S. Hirata, H. Miyazaki, C. Adachi, *J. Am. Chem. Soc.* **2012**, *134*, 14706–14709.
[17] L. Zhan, Y. Xiang, Z. Chen, K. Wu, S. Gong, G. Xie, C. Yang, *J. Mater. Chem. C* **2019**, *7*, 13953–13959.
[18] X. Zeng, K.-C. Pan, W.-K. Lee, S. Gong, F. Ni, X. Xiao, W. Zeng, Y. Xiang, L. Zhan, Y. Zhang, C.-C. Wu, C. Yang, *J. Mater. Chem. C* **2019**, *7*, 10851–10859.
[19] D. H. Ahn, S. W. Kim, H. Lee, I. J. Ko, D. Karthik, J. Y. Lee, J. H. Kwon, *Nat. Photonics* **2019**, *13*, 540–546.
[20] X. Liang, H. B. Han, Z. P. Yan, L. Liu, Y. X. Zheng, H. Meng, W. Huang, *New J. Chem.* **2018**, *42*, 4317–4323.
[21] S. Ye, S. Zhuang, B. Pan, R. Guo, L. Wang, *J. Inf. Disp.* **2020**, *21*, 173–196.
[22] W.-C. Chen, Z.-L. Zhu, C.-S. Lee, *Adv. Opt. Mater.* **2018**, *6*, 1800258.
[23] R.-H. Yi, C.-M. Shao, C.-H. Lin, Y.-C. Fang, H.-L. Shen, C.-W. Lu, K.-Y. Wang, C.-H. Chang, L.-Y. Chen, Y.-H. Chang, *J. Phys. Chem. C* **2020**, *124*, 20410–20423.
[24] Y. Liu, L. Yang, Q. Bai, W. Li, Y. Zhang, Y. Fu, F. Ye, *Chem. Eng. J.* **2021**, *420*, 129939.
[25] Z. Zhang, Y. Li, X. Wu, W. Chu, S. Yin, *J. Mater. Chem. C* **2020**, *8*, 11239–11251.
[26] J. Devesing Girase, S. Rani Nayak, J. Tagare, Shahnawaz, M. Ram Nagar, J.-H. Jou, S. Vaidyanathan, *J. Inf. Disp.* **2022**, *23*, 53–67.
[27] A. Pachariyangkun, W. Senapak, T. Sudyoadsuk, S. Namuangruk, V. Promarak, *Org. Electron.* **2020**, *85*, 105897.
[28] Y. Liu, H. Liu, Q. Bai, C. Du, A. Shang, D. Jiang, X. Tang, P. Lu, *ACS Appl. Mater. Interfaces* **2020**, *12*, 16715–16725.
[29] P. Yu, Y. Xiao, *Materials* **2021**, *14*, 2349.
[30] K. Usman, A. Islam, S. H. Ullah Shah, K. Javaid, A. Amin, Z. Mustafa, A. G. Wattoo, N. Abbas, Z. Ge, *Opt. Mater.* **2021**, *121*, 111582.
[31] R. H. Yi, G. Y. Liu, Y. T. Luo, W. Y. Wang, H. Y. Tsai, C. H. Lin, H. L. Shen, C. H. Chang, C. W. Lu, *Chem. Eur. J.* **2021**, *27*, 12998–13008.
[32] T. Ohsawa, H. Sasabe, T. Watanabe, K. Nakao, R. Komatsu, Y. Hayashi, Y. Hayasaka, J. Kido, *Adv. Opt. Mater.* **2019**, *7*, 1801282.
[33] Y. Kusakabe, Y. Wada, T. Misono, K. Suzuki, K. Shizu, H. Kaji, *ACS Omega* **2022**, *7*, 16740–16745.
[34] D. Thakur, M. R. Nagar, A. Tomar, D. K. Dubey, S. Kumar, S. S. Swayamprabha, S. Banik, J. Jou, S. Ghosh, *ACS Appl. Electron. Mater.* **2021**, *3*, 2317–2332.
[35] S. Grimme, *Chem. Phys. Lett.* **1996**, *259*, 128–137.
[36] H. Debus, *Annalen der Chemie und Pharmacie* **1858**, *107*, 199–208.
[37] Br. Radziszewski, *Ber. Dtsch. Chem. Ges.* **1882**, *15*, 1493–1496.
[38] P. A. Forero-Cortés, A. M. Haydl, *Org. Process Res. Dev.* **2019**, *23*, 1478–1483.
[39] A. B. Kajjam, D. K. Dubey, R. A. Kumar Yadav, J.-H. Jou, V. Sivakumar, *Materials Today Chemistry* **2019**, *14*, 100201; B. Zhao, Z.-Y. Li, M.-J. Fan, B. Song, Q.-G. Deng, *Acta Crystallographica Section E: Structure Reports Online* **2012**, *68*, o542, 10.1107/S1600536812003145; R. Vaid, M. Gupta, G. Kour, V. K. Gupta, *Chemistry Select* **2019**, *4*, 9179, 10.1002/slct.201902012.
[40] J. A. Pople, J. S. Binkley, R. Seeger, *Int. J. Quantum Chem.* **2009**, *10*, 1–19.
[41] J. P. Perdew, M. Ernzerhof, K. Burke, *J. Chem. Phys.* **1996**, *105*, 9982–9985.
[42] S. Hirata, M. Head-Gordon, *Chem. Phys. Lett.* **1999**, *314*, 291–299.
[43] A. B. Kajjam, D. K. Dubey, R. A. Kumar Yadav, J.-H. Jou, V. Sivakumar, *Materials Today Chemistry* **2019**, *14*, 100201.
[44] G. Gritzner, J. Kuta, *Pure Appl. Chem.* **1984**, *56*, 461–466.
[45] N. G. Connelly, W. E. Geiger, *Chem. Rev.* **1996**, *96*, 877–910.
[46] C. M. Cardona, W. Li, A. E. Kaifer, D. Stockdale, G. C. Bazan, *Adv. Mater.* **2011**, *23*, 2367–2371.
[47] J. Rigaku Americas, The Woodlands, Texas, USA, and Rigaku Corporation, Tokyo, **2015**.
[48] U. K. CrysAlisPro v1.171.38.46. Rigaku Oxford Diffraction, Rigaku Corporation, Oxford, **2015**.

[49] M. C. Burla, R. Caliandro, M. Camalli, B. Carrozzini, G. L. Cascarano, C. Giacovazzo, M. Mallamo, A. Mazzone, G. Polidori, R. Spagna, *J. Appl. Crystallogr.* **2012**, *45*, 357–361.
[50] G. M. Sheldrick, *Acta Crystallogr. Sect. C* **2015**, *71*, 3–8.
[51] O. V. Dolomanov, L. J. Bourhis, R. J. Gildea, J. A. K. Howard, H. Puschmann, *J. Appl. Crystallogr.* **2009**, *42*, 339–341.
[52] J. A. Pople, J. S. Binkley, R. Seeger, *Int. J. Quantum Chem.* **1976**, *10*, 1–19.
[53] S. Grimme, *Chem. Phys. Lett.* **1996**, *259*, 128–137.
[54] J. Tomasi, B. Mennucci, R. Cammi, *Chem. Rev.* **2005**, *105*, 2999–3094.
[55] G. S. Frisch, M. J. Trucks, G. W. Schlegel, H. B. Scuseria, G. E. Robb, M. A. Cheeseman, J. R. Scalmani, G. Barone, V. Mennucci, B. Petersson, G. A. Nakatsuji, H. Caricato, M. Li, X. Hratchian, H. P. Izmaylov, A. F. Bloino, J. Zheng, *Gaussian 09, Revis. D.01. Wallingford, CT* **2009**.
[56] GaussView, Version 6.1.1, Roy Dennington, Todd Keith, and John Millam, Semichem Inc., Shawnee Mission, KS, **2019**.
[57] N. M. O'Boyle, A. L. Tenderholt, K. M. Langner, *J. Comput. Chem.* **2008**, *29*, 839–845.
[58] M. Moral, L. Muccioli, W.-J. Son, Y. Olivier, J. C. Sancho-García, *J. Chem. Theory Comput.* **2015**, *11*, 168–177.
[59] N. G. Connelly, W. E. Geiger, *Chem. Rev.* **1996**, *96*, 877–910.
[60] N. C. Greenham, I. D. W. Samuel, G. R. Hayes, R. T. Phillips, Y. A. R. R. Kessener, S. C. Moratti, A. B. Holmes, R. H. Friend, *Chem. Phys. Lett.* **1995**, *241*, 89–96.

Submitted: January 24, 2023
Accepted: February 9, 2023